



# Tunable topological phase transition in the telecommunication wavelength

FANGLIN TIAN,<sup>1,†</sup> JUNXIAO ZHOU,<sup>1,†</sup> QIANG WANG,<sup>2</sup> AND ZHAOWEI LIU<sup>1,\*</sup> 

<sup>1</sup>*Department of Electrical and Computer Engineering, University of California, San Diego, 9500 Gilman Drive, La Jolla, California 92093, USA*

<sup>2</sup>*Division of Physics and Applied Physics, School of Physical and Mathematical Sciences, Nanyang Technological University, Singapore*

<sup>†</sup>These authors contributed equally to this work.

\*[zhaowei@ucsd.edu](mailto:zhaowei@ucsd.edu)

**Abstract:** Recent progress in the Valley Hall insulator has demonstrated a nontrivial topology property due to the distinct valley index in 2D semiconductor systems. In this work, we propose a highly tunable topological phase transition based on valley photonic crystals. The topological phase transition is realized by the inversion symmetry broken due to the refractive index change of structures consisting of optical phase change material (OPCM) with thermal excitation of different sites in a honeycomb lattice structure. Besides, simulations of light propagation at sharp corners and pseudo-spin photon coupling are conducted to quantitatively examine the topological protection. Compared with other electro-optical materials based on reconfigurable topological photonics, a wider bandwidth and greater tunability of both central bandgap frequency and topological phase transition can happen in the proposed scheme. Our platform has great potential in practical applications in lasing, light sensing, and high-contrast tunable optical filters.

© 2023 Optica Publishing Group under the terms of the [Optica Open Access Publishing Agreement](#)

Topological insulators (TIs) offer the possibility of maintaining electron flow on their surface while keeping insulating in their interior. These unique surface states are robust under the presence of surface defects and disorders [1,2]. The underlying physical origin of this unusual surface behavior can be related to the topological invariant of the system-Chern number, which represents the topological nature of eigenfunction over the whole Brillouin Zone [3]. Photonic analogues of TIs (PTIs) were first realized in microwave frequency by applying strong magnetic field to break the time-reversal symmetry [4]. Later, various strategies of utilizing the valley and spin degree of freedoms were proposed in plasmonic [5,6] and dielectric material platforms [7–9], where time-reversal symmetry preserves. Through all the attempts, harvesting the extra valley degree of freedoms in honeycomb lattice shows great application potential in all major photonic devices like optical switching [10,11], lasing [12,13], communications [14,15] and nonlinear optics [16,17] on account of the balance between fabrication tolerance and topological protection strength. For most application scenarios, operating wavelength and tunability of topological protection edge states is of great importance. Nevertheless, majority of current systems can only work at given modes of operation and fixed frequency. Several attempts had been made for dynamically tuning of PTIs by using the Kerr-type optical nonlinearity [18], liquid crystal variation [19] and mechanical control [20]. However, they are suffering from very high operational peak power, large footprint and limited tunable bandwidth problems.

Optical phase changing material (OPCM) is a unique group of material that has at least two different phase states (commonly known as amorphous and crystalline) and can be reversely modulated between them. With external excitation, OPCM demonstrates significant change of optical property under different material phases [21,22]. This extraordinary optical behavior promises OPCMs' application capability in tunable optical devices including but not limited to

optical switching [23–26], programmable metasurfaces [27,28], tunable light emitters [29,30], thermal rectification [31], and absorbers [32,33]. Among most existing OPCMs, chalcogen-based alloys demonstrated promising properties including fast switching ( $< 100$  ns), extreme robustness (potentially up to  $10^{12}$  cycles) and energy-efficient switching ( $\sim 10$  aJ/nm<sup>3</sup>) [34]. Within the chalcogen-based OPCMs family, the optical figure of merit (i. e.,  $\Delta n/\Delta k$ ) of Sb<sub>2</sub>Se<sub>3</sub> outperforms most of other competitors benefiting from its ultra-low optical loss ( $k < 10^{-5}$ ) at telecommunication wavelength, which can truly become a strong candidate in optical industry [35].

Given that, we propose a reconfigurable PTI device based on a valley photonic crystal using Sb<sub>2</sub>Se<sub>3</sub> as the active medium for topological photonic crystal. By heating half of the sublattice in honeycomb lattice, the degeneracy of Dirac cone is lift due to the breaking of inversion symmetry, and host non-trivial valley Chern number. It realizes robust light propagation at sharp corners and the unidirectional coupling of circular polarized light without modifying the geometrical setup. The tunability of propagation properties is facilitated by the refractive index change of the PTI structures due to thermal excitation. In contrast to most of the reconfigurable topological photonics works, this special design offers dynamical switching between topological trivial and non-trivial phase and topological interface reconfiguration ability within the same structure at telecommunication wavelength and can be extended to other frequencies. This structure can be used to construct integrated on-chip high-speed photonic devices, leading to promising applications at optical communication wavelengths.

As demonstrated in Fig. 1(a), the topological photonic crystal consists of mirrored-symmetry honeycomb lattices made of Sb<sub>2</sub>Se<sub>3</sub> nanorods (PC1 and PC2 in Fig. 1(a)) as the active medium in our design. The rhomboid shaped unit cell has a periodicity of  $a = 408$  nm and the diameter of two identical rods is  $d = 195$  nm. The height of Sb<sub>2</sub>Se<sub>3</sub> rods is chosen as  $h = 815$  nm so that photonic bandgap at valley point can be large enough to support interface states without having higher order mode involved [36]. The combination of structure parameters is selected in such a way that the edge state is located well below the light cone, which guarantees the in-plane light confinement. Silver electrodes are used to sandwich the AlN layer, enabling high spatial resolution heat dissipation. The heaters are placed under the red sites of the photonic crystal [Fig. 1(b)] while providing enough space between the Sb<sub>2</sub>Se<sub>3</sub> rods and heater to ensure that the photonic modes are not impacted by the heater. The design could be experimentally realized using standard cleanroom process including photolithography, material deposition (sputtering, ALD, etc.), chemical mechanical polishing and wet etching. Pulse current source is connected to the two electrodes of heater and material phase of OPCM can be dynamically tuned based on current's temporal response [37,38]. The blue rods will remain at amorphous state of Sb<sub>2</sub>Se<sub>3</sub> constantly. The material phase of red rods can be tuned between amorphous and crystalline states stem from pulse current. The symmetry of each photonic crystal lattice can be dynamically adjusted from  $C_{6v}$  to  $C_{3v}$  thanks to inversion symmetry breaking which are termed as “symmetric TM mode” (SM) and “symmetric breaking TM mode” (SBM) here, and the topological photonic boundary consists of two mirrored photonic crystal can be created to support light propagation.

The schematic crystal structure of Sb<sub>2</sub>Se<sub>3</sub> is shown in Fig. 1(c). The optical contrast between amorphous and crystalline states may arise from a loss of medium-range order and resonant bonding in the amorphous phase [39]. The ellipsometry measurement results used in this work are adopted from Ref. [40], as shown in Fig. 1(d). In this work, we focus on telecommunication wavelength, due to a large refractive index change  $\Delta n = 0.77$  and minor optical loss.

The valley dependent topological nature in honeycomb lattice has been theoretically investigated and experimentally verified in both electrical and photonic systems [41–43]. Near the Dirac cone, the effective massive Hamiltonian  $\mathcal{H}_{eff} = \mathcal{H}_0 + H_p$  can be expanded to its first order approximation subject to symmetry constraints

$$\mathcal{H}_{eff} = v_g(\delta k_x \tau_z \sigma_x s_0 + \delta k_y \tau_0 \sigma_y s_0) + m_{eff} \tau_0 s_0 \sigma_z \quad (1)$$

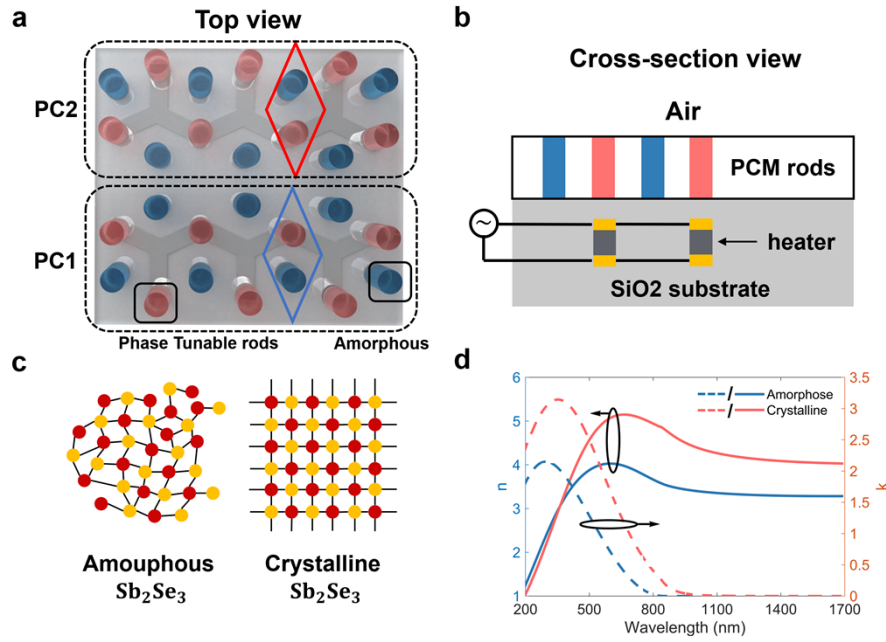


**Fig. 1.** Schematic figure of the proposed tunable valley photonic crystal. (a) The designed structure contains two sites of mirrored valley photonic crystals. Unit cell: blue (red) rhombic for PC1 (PC2) with heater driven by electrical pulse source under the structure. The unit cell of both mirrored photonic crystal is shown in the parallelogram. (b) Cross section view of the designed structure. (c) Schematic illustration of amorphous and crystalline  $\text{Sb}_2\text{Se}_3$ . (d) Wavelength dependent refractive index of  $\text{Sb}_2\text{Se}_3$  of different phase conditions.

$\mathcal{H}_0$  is the massless unperturbed Hamiltonian and the inversion symmetry breaking gives a perturbation matrix  $\mathcal{H}_p$ . Here,  $v_g$  is the group velocity,  $\delta k = (\delta k_x, \delta k_y)$  is the momentum distance from the Dirac point,  $\sigma_{x,y,z}$ ,  $\tau_{x,y,z}$  and  $s_{x,y,z}$  are Pauli matrices acting on orbital, valley and polarization state vector,  $\tau_0$ ,  $\sigma_0$ ,  $s_0$  are the corresponding unit matrixes and  $m_{eff}$  is the effective mass term. The eigenvalue of the massive Dirac Hamiltonian is given by  $E(\delta k) = \pm \sqrt{\sum_i (v_g^2 \delta k_i^2 + m_{eff}^2)}$  around the Dirac frequency. It's clear enough that any non-zero effective mass term can gap the Dirac cone which represents the inversion symmetry breaking between the rods. Also, the two Dirac Hamiltonians around K (K') correspond to two different valley pseudospins (up/down). This extra valley degree of freedom is quite useful in dealing with the actual photonic system where our design is based on.

The simulated dispersion of both proposed PC1 and PC2 is shown in Fig. 2(a) (all simulations are performed using COMSOL Multiphysics). In this work, we will only focus on TM polarization unless special noted. As PC1 and PC2 are mirrored symmetrical structures, they share the same band structure with opposite valley Chern number. When the material phase of  $\text{Sb}_2\text{Se}_3$  rods with heater beneath is amorphous (SM configuration), there's no TM bandgap opening since the inversion symmetry is reserved. The Dirac points at the K and K' points of the Brillouin zone have a frequency of 221 THz. The interface connects two mirrored photonic crystals doesn't support any kind of boundary modes in this configuration. When the material phase of  $\text{Sb}_2\text{Se}_3$  rods with heater beneath is excited to be crystalline (SBM configuration), the inversion symmetry breaking happens between two sites as the refractive index differences arise. A significant TM-like polarization bandgap ( $\sim 8\%$ ) opens between 188 THz and 204 THz, and the interface

between the two mirrored photonic crystals support topological edge state which will show in the next section.

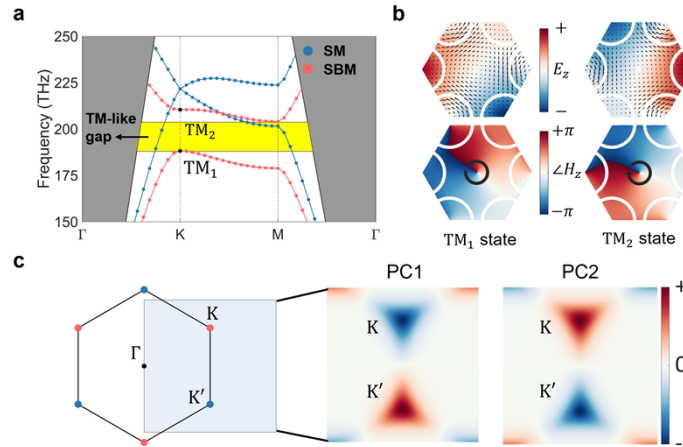


**Fig. 2.** Valley photonic crystal band structure and non-trivial topology. (a) Bulk band structure of photonic crystal at different states. Blue line: symmetric TM mode (SM). Red line: symmetric breaking TM mode (SBM). Yellow region: TM-like bandgap. Grey region: Light cone of SiO<sub>2</sub> substrate. (b) Simulated  $E_z$  field and phase vortex of  $H_z$  field at K point for two lowest TM-like band in band structure. The black arrows indicate the Poynting power flow, and the vector rotates CW/CCW at TM<sub>1</sub>/TM<sub>2</sub> states. (c) Berry curvature distribution at K/K' point for two mirrored valley photonic crystal at symmetric breaking mode (topological nontrivial).

Additionally, we can have more intuitive understanding about the topological nature from the eigenstates of PC1 and PC2. Since the topological non-trivial property only exists when the material phase is different between the two types of rods in each unit cell, we will mainly focus on the topological property in this inversion symmetry broken state. Taking the lowest two TM-like polarization band (TM<sub>1</sub> and TM<sub>2</sub> in Fig. 2(a)) at K point as example, the simulated electrical fields along z direction ( $E_z$ ) at  $xy$  plane located at middle of PCM rods are shown in the upper panel of upper Fig. 2(b). It's evident that electrical field mainly concentrates on the higher index rods at lower energy eigenstates (TM<sub>1</sub> in Fig. 2(b)), whereas shifts to opposite sites at higher energy eigenstates (TM<sub>2</sub> in Fig. 2(b)). Poynting vectors show that the energy flows rotate clockwise (CW)/ counterclockwise (CCW) at TM<sub>1</sub>-state and TM<sub>2</sub>-state, respectively. It can also be verified in the simulated phase profile of magnetic field. The magnetic field phase increases by  $2\pi$  CW/CCW around the center of unit cell. This vortex-like phenomenon is related to the valley dependent pseudospin property in condensed matter system and exists as photonic valley pseudospin. Like in transition metal dichalcogenides, the photonic valley also depends on chirality of excitation light [44].

The mentioned Dirac Hamiltonian and phase vortex can be related to the non-trivial topological phase of this setup. To find out the topology nature of structure, we perform analysis of the Berry curvature over more than a quarter of Brillouin zone. The designed structure features a non-zero Berry curvature with opposite sign at K/K' point when the material phases between two types of rods are different. The gauge invariant Berry curvature can be calculated by  $\Omega_n(k) = \nabla_k \times A_n(k)$ , where  $A_n(k)$  is the gauge dependent Berry connection for  $n$ th band. Berry connection is defined as  $A_n(k) \equiv i \langle u_{n,k} | \nabla_k | u_{n,k} \rangle$ , where  $u_{n,k}$  is the normalized Bloch state which obeys the same periodicity as the original Hamiltonian. In two-dimensional photonic crystal system, the Berry curvature

only has one component:

$$\Omega_n(\mathbf{k}) = i(\langle \partial_{k_x} \mathbf{u}_{n,\mathbf{k}} | \partial_{k_y} \mathbf{u}_{n,\mathbf{k}} \rangle - \langle \partial_{k_y} \mathbf{u}_{n,\mathbf{k}} | \partial_{k_x} \mathbf{u}_{n,\mathbf{k}} \rangle) \quad (2)$$

The distribution of Berry curvatures calculated for the lowest TM-like band of PC1 and PC2 in SBM configuration are shown in Fig. 2(c). The Berry curvature is mainly distributed around K and K' points. Note that the sign of Berry curvature distribution at K and K' points is opposite, and PC2 reverses the Berry curvature distribution compared with PC1. Meanwhile, the integral of Berry curvature over the whole Brillouin Zone (Chern number) strictly equals to zero as the reserved time-reversal symmetry. Conversely, the Berry curvature distributions for PC1 and PC2 are topological trivial and identical when the material phase of two rods are uniform (SM configuration) which indicate the inversion symmetry is preserved. In this case, the structure is gapless. By changing the material phase of one of the rods in unit cell, we can realize topological phase transition, providing an effective way to retrieve the topological properties in photonic system.

To further comprehend the topological nature of this valley photonic crystal, we build a topological interface with PC1 and PC2 shown in Fig. 3(a). In this boundary design, two opposite photonic crystals sit next to each other and share the same photonic bandgap. We will mainly focus on the SBM case when material phase of different rods in both mirrored photonic crystals are different since there's no topological non-trivial property in reserved inversion symmetry case. The Zigzag interface and material phase of  $\text{Sb}_2\text{Se}_3$  rods configuration is chosen to maximize the below light cone interface state bandwidth. Figure 3(b) shows the interface band structure where an edge state connects the TM-like bandgap with negative group velocity at K point. Due to the inversion symmetry condition in Brillouin Zone, a reversed edge state with opposite velocity will exist at another valley. Detailed field distribution of the interface with a specific wavevector is also shown in Fig. 3(b).

To confirm the performance of topological edge state with sharp turns, we build the photonic crystal structure with different geometrical configurations and study the light propagation in them. It shows that the propagation is robust under sharp turns and its transmission efficiency maintains high without being affected by the shape of waveguide design, as shown Fig. 3 (c) and (d). These results provide solid proof that the propagation of light along the edge between mirrored symmetry topological photonic crystal is protected from scattering at sharp turns. By contrast, the light propagates disorderly when all the rods are in the same material phase (SM mode) and no topological nontrivial boundary mode are supported (Fig. 3(d) right)). Note that we use an effective index approximation method to simplify the three-dimensional problem to two dimensional [45,46].

As another important topological property, unidirectional routing can be used to manipulate the injection direction of light naturally. Here, we use the same boundary setup as discussed in the previous section. The injection light source is placed at one of the boundary rods where efficient unidirectional coupling can be realized due to the inversion symmetry breaking at the interface [Fig. 4(a)]. When the boundary of structure is excited by linear polarized dipole source [Fig. 4(b)], the electromagnetic energy flows equally to both sides of interface waveguide. While for circular polarized light dipole source, leftward / rightward propagation takes place as expected from the favor of bulk topology [Fig. 4(c) and (d)]. Shift half a lattice constant can be used to increase the chiral source coupling efficiency further [47]. In addition, all-optical integration can be achieved with the help of subwavelength on-chip microdisk, which distinguishes the handedness of incoming circularly polarized light beam [48]. This results clearly show the existence of non-trivial topological property in the designed structure.

We have proposed and demonstrated the performance of an optical phase transition material based topological photonic crystal, which shows topological phase transition possibility and valley Hall effect at telecommunication wavelength in topological non-trivial state. Inversion

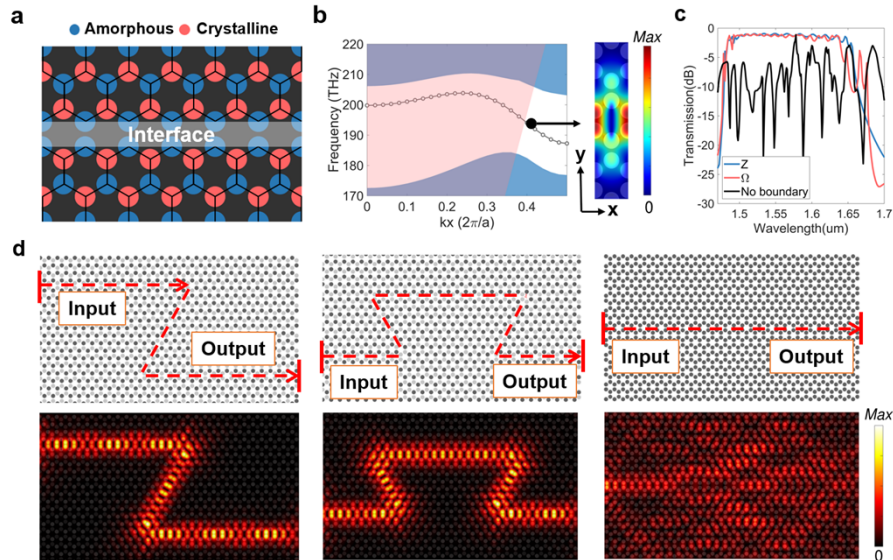


**Fig. 3.** Topological interface propagation. (a) Schematic of Zigzag boundary setup. Amorphous state rods are arranged at the interface to maximize the bandwidth. (b) Interface states dispersion (left) of the periodic 3D structure illustrated in (a) and boundary field distribution (right). (c) Transmission efficiency for 2D Z/ $\Omega$  shape interface setup and no topological boundary setup. (d) Simulated normalized electrical field distribution in Z,  $\Omega$  and line shape interfaces with SBM (left & middle) and SM configuration (right). The port position is indicated by red line at the boundary.

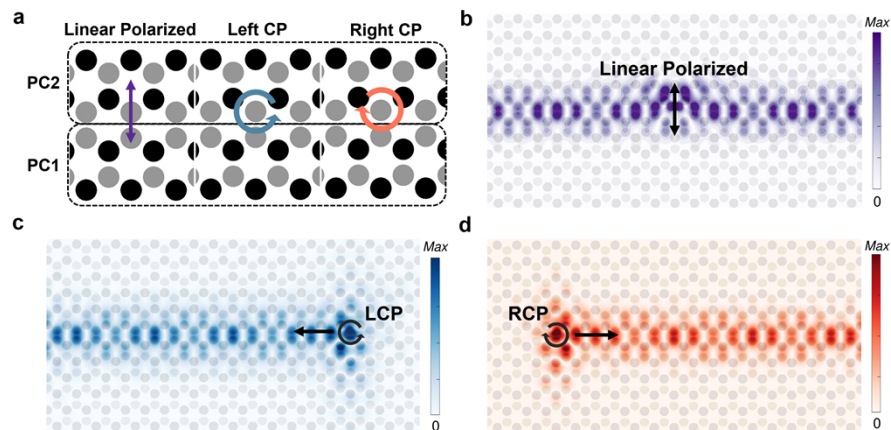


**Fig. 4.** Topological edge states excited by light source with opposite angular momentum. (a) Simulated energy distribution for linear polarized (b), left- (c) and right-handed polarized (d), i.e., LCP and RCP, light injection at one of the boundary rods. For linear polarized input light, energy distribute equally to both direction of boundary, whereas for LCP/RCP light, energy only couple to one direction which is related to the boundary topological property.

symmetry breaking in the structure is realized by asymmetrical thermal excitation in the unit cell and can be reversely tuned back and forth. Robust propagation and unidirectional coupling are numerically verified and optimized to its best performance. Our work may open a new route to tunable topological photonic devices and could potentially stimulate the application of topological photonic in tunable integrated photonic circuits.

**Funding.** National Science Foundation (NSF-ECCS-1907423).

**Disclosures.** The authors declare no conflicts of interest.

**Data availability.** Data underlying the results presented in this paper are not publicly available at this time but may be obtained from the authors upon reasonable request.

## References

1. J. E. Moore, "The birth of topological insulators," *Nature* **464**(7286), 194–198 (2010).
2. L. Lu, J. D. Joannopoulos, and M. Soljačić, "Topological photonics," *Nat. Photonics* **8**(11), 821–829 (2014).
3. T. Ozawa, H. M. Price, A. Amo, N. Goldman, M. Hafezi, L. Lu, M. C. Rechtsman, D. Schuster, J. Simon, and O. Zilberberg, "Topological photonics," *Rev. Mod. Phys.* **91**(1), 015006 (2019).
4. Z. Wang, Y. Chong, J. D. Joannopoulos, and M. Soljačić, "Observation of unidirectional backscattering-immune topological electromagnetic states," *Nature* **461**(7265), 772–775 (2009).
5. J. You, Q. Ma, Z. Lan, Q. Xiao, N. C. Panoiu, and T. Cui, "Reprogrammable plasmonic topological insulators with ultrafast control," *Nat. Commun.* **12**(1), 5468 (2021).
6. X. Wu, Y. Meng, J. Tian, Y. Huang, H. Xiang, D. Han, and W. Wen, "Direct observation of valley-polarized topological edge states in designer surface plasmon crystals," *Nat. Commun.* **8**(1), 1304 (2017).
7. X. He, E. Liang, J. Yuan, H. Qiu, X. Chen, F. Zhao, and J. Dong, "A silicon-on-insulator slab for topological valley transport," *Nat. Commun.* **10**(1), 872 (2019).
8. J. Dong, X. Chen, H. Zhu, Y. Wang, and X. Zhang, "Valley photonic crystals for control of spin and topology," *Nat. Mater.* **16**(3), 298–302 (2017).
9. X. Gao, L. Yang, H. Lin, L. Zhang, J. Li, F. Bo, Z. Wang, and L. Lu, "Dirac-vortex topological cavities," *Nat. Nanotechnol.* **15**(12), 1012–1018 (2020).
10. M. I. Shalaev, W. Walasik, and N. M. Litchinitser, "Optically tunable topological photonic crystal," *Optica* **6**(7), 839–844 (2019).
11. L. He, W. Zhang, and X. Zhang, "Topological all-optical logic gates based on two-dimensional photonic crystals," *Opt. Express* **27**(18), 25841–25859 (2019).
12. D. Smirnova, A. Tripathi, S. Kruk, M.-S. Hwang, H.-R. Kim, H.-G. Park, and Y. Kivshar, "Room-temperature lasing from nanophotonic topological cavities," *Light: Sci. Appl.* **9**(1), 127 (2020).
13. X.-C. Sun and X. Hu, "Topological ring-cavity laser formed by honeycomb photonic crystals," *Phys. Rev. B* **103**(24), 245305 (2021).
14. A. Kumar, M. Gupta, P. Pitchappa, N. Wang, M. Fujita, and R. Singh, "Terahertz topological photonic integrated circuits for 6 G and beyond: a perspective," *J. Appl. Phys.* **132**(14), 140901 (2022).
15. A. Kumar, M. Gupta, P. Pitchappa, N. Wang, P. Szriftgiser, G. Ducournau, and R. Singh, "Phototunable chip-scale topological photonics: 160 Gbps waveguide and demultiplexer for THz 6 G communication," *Nat. Commun.* **13**(1), 5404 (2022).
16. D. Smirnova, S. Kruk, D. Leykam, E. Melik-Gaykazyan, D.-Y. Choi, and Y. Kivshar, "Third-harmonic generation in photonic topological metasurfaces," *Phys. Rev. Lett.* **123**(10), 103901 (2019).
17. J. Noh, W. A. Benalcazar, S. Huang, M. J. Collins, K. P. Chen, T. L. Hughes, and M. C. Rechtsman, "Topological protection of photonic mid-gap defect modes," *Nat. Photonics* **12**(7), 408–415 (2018).
18. Z. Hu, D. Bongiovanni, D. Jukić, E. Jajtić, S. Xia, D. Song, J. Xu, R. Morandotti, H. Buljan, and Z. Chen, "Nonlinear control of photonic higher-order topological bound states in the continuum," *Light: Sci. Appl.* **10**(1), 164 (2021).
19. M. I. Shalaev, S. Desnani, W. Walasik, and N. M. Litchinitser, "Reconfigurable topological photonic crystal," *New J. Phys.* **20**(2), 023040 (2018).
20. Z. Gao, Z. Yang, F. Gao, H. Xue, Y. Yang, J. Dong, and B. Zhang, "Valley surface-wave photonic crystal and its bulk/edge transport," *Phys. Rev. B* **96**(20), 201402 (2017).
21. M. N. Julian, C. Williams, S. Borg, S. Bartram, and H. J. Kim, "Reversible optical tuning of GeSbTe phase-change metasurface spectral filters for mid-wave infrared imaging," *Optica* **7**(7), 746–754 (2020).
22. X. Shi, C. Chen, S. Liu, and G. Li, "Nonvolatile and reconfigurable tuning of surface lattice resonances using phase-change Ge<sub>2</sub>Sb<sub>2</sub>Te<sub>5</sub> thin films," *Results Phys.* **22**, 103897 (2021).
23. Y. Zhang, J. B. Chou, and J. Li, *et al.*, "Broadband transparent optical phase change materials for high-performance nonvolatile photonics," *Nat. Commun.* **10**(1), 4279 (2019).
24. C. Zhang, M. Zhang, Y. Xie, Y. Shi, R. Kumar, R. R. Panepucci, and D. Dai, "Wavelength-selective 2×2 optical switch based on a Ge<sub>2</sub>Sb<sub>2</sub>Te<sub>5</sub>-assisted microring," *Photonics Res.* **8**(7), 1171–1176 (2020).
25. R. R. Ghosh and A. Dhawan, "Numerical modeling of an integrated non-volatile reflector switch and mode converter switch based on a low loss phase change material (Sb<sub>2</sub>Se<sub>3</sub>) in SiN platforms," *Opt. Mater. Express* **12**(11), 4268–4283 (2022).

26. J. Xu, X. Tian, Z.-Y. Li, K. Xu, P. Ding, Z. Yu, and Y. Du, "Ge<sub>2</sub>Sb<sub>2</sub>Se<sub>4</sub>Te<sub>1</sub>-based spin-decoupled metasurface for multidimensional and switchable focusing in the mid-infrared regime," *Opt. Mater. Express* **12**(3), 918–930 (2022).
27. N. Raeis-Hosseini and J. Rho, "Metasurfaces based on phase-change material as a reconfigurable platform for multifunctional devices," *Materials* **10**(9), 1046 (2017).
28. C. Ding, G. Rui, B. Gu, Q. Zhan, and Y. Cui, "Phase-change metasurface with tunable and switchable circular dichroism," *Opt. Lett.* **46**(10), 2525–2528 (2021).
29. K.-K. Du, Q. Li, Y.-B. Lyu, J.-C. Ding, Y. Lu, Z.-Y. Cheng, and M. Qiu, "Control over emissivity of zero-static-power thermal emitters based on phase-changing material GST," *Light: Sci. Appl.* **6**(1), e16194 (2016).
30. Y. Qu, L. Cai, H. Luo, J. Lu, M. Qiu, and Q. Li, "Tunable dual-band thermal emitter consisting of single-sized phase-changing GST nanodisks," *Opt. Express* **26**(4), 4279–4287 (2018).
31. Y. Liu, A. Caratenuto, and Y. Zheng, "GST-VO<sub>2</sub>-based near-field multistage radiative thermal rectifier," *Opt. Mater. Express* **12**(6), 2135–2144 (2022).
32. M. Pourmand, P. Choudhury, and M. A. Mohamed, "Tunable absorber embedded with GST mediums and trilayer graphene strip microheaters," *Sci. Rep.* **11**(1), 3603 (2021).
33. C. Ríos, M. Stegmaier, P. Hosseini, D. Wang, T. Scherer, C. D. Wright, H. Bhaskaran, and W. H. Pernice, "Integrated all-photonic non-volatile multi-level memory," *Nat. Photonics* **9**(11), 725–732 (2015).
34. F. Xiong, A. D. Liao, D. Estrada, and E. Pop, "Low-power switching of phase-change materials with carbon nanotube electrodes," *Science* **332**(6029), 568–570 (2011).
35. K. V. Sreekanth, Q. Ouyang, S. Sreejith, S. Zeng, W. Lishu, E. Ilker, W. Dong, M. ElKabbash, Y. Ting, and C. T. Lim, "Phase-change-material-based low-loss visible-frequency hyperbolic metamaterials for ultrasensitive label-free biosensing," *Adv. Opt. Mater.* **7**(12), 1900081 (2019).
36. J.D. Joannopoulos, S.G. Johnson, J.N. Winn, and R.D. Meade, in *Photonic Crystals: Molding the Flow of Light* (Princeton University Press, 2011).
37. Y. Wang, P. Landreman, D. Schoen, K. Okabe, A. Marshall, U. Celano, H.-S. P. Wong, J. Park, and M. L. Brongersma, "Electrical tuning of phase-change antennas and metasurfaces," *Nat. Nanotechnol.* **16**(6), 667–672 (2021).
38. J. Faneca, L. Trimby, I. Zeimpekis, M. Delaney, D. W. Hewak, F. Y. Gardes, C. D. Wright, and A. Baldycheva, "On-chip sub-wavelength Bragg grating design based on novel low loss phase-change materials," *Opt. Express* **28**(11), 16394–16406 (2020).
39. D. Lencer, M. Salinga, B. Grabowski, T. Hickel, J. Neugebauer, and M. Wuttig, "A map for phase-change materials," *Nat. Mater.* **7**(12), 972–977 (2008).
40. M. Delaney, I. Zeimpekis, D. Lawson, D. W. Hewak, and O. L. Muskens, "A new family of ultralow loss reversible phase-change materials for photonic integrated circuits: Sb<sub>2</sub>S<sub>3</sub> and Sb<sub>2</sub>Se<sub>3</sub>," *Adv. Funct. Mater.* **30**(36), 2002447 (2020).
41. F. Gao, H. Xue, Z. Yang, K. Lai, Y. Yu, X. Lin, Y. Chong, G. Shvets, and B. Zhang, "Topologically protected refraction of robust kink states in valley photonic crystals," *Nat. Phys.* **14**(2), 140–144 (2018).
42. T. Ma and G. Shvets, "All-Si valley-Hall photonic topological insulator," *New J. Phys.* **18**(2), 025012 (2016).
43. G. Wei, Z. Liu, L. Wang, J. Song, and J.-J. Xiao, "Coexisting valley and pseudo-spin topological edge states in photonic topological insulators made of distorted Kekulé lattices," *Photonics Res.* **10**(4), 999–1010 (2022).
44. H. Zeng, J. Dai, W. Yao, D. Xiao, and X. Cui, "Valley polarization in MoS<sub>2</sub> monolayers by optical pumping," *Nat. Nanotechnol.* **7**(8), 490–493 (2012).
45. M. Qiu, "Effective index method for heterostructure-slab-waveguide-based two-dimensional photonic crystals," *Appl. Phys. Lett.* **81**(7), 1163–1165 (2002).
46. M. Hammer and O. V. Ivanova, "Effective index approximations of photonic crystal slabs: a 2-to-1-D assessment," *Opt. Quantum Electron.* **41**(4), 267–283 (2009).
47. A. Mock, L. Lu, and J. O'Brien, "Space group theory and Fourier space analysis of two-dimensional photonic crystal waveguides," *Phys. Rev. B* **81**(15), 155115 (2010).
48. F. J. Rodriguez-Fortuno, I. Barber-Sanz, D. Puerto, A. Griol, and A. Martínez, "Resolving light handedness with an on-chip silicon microdisk," *ACS Photonics* **1**(9), 762–767 (2014).